Are charged tips driving TERS-resolution? A full quantum chemical approach

K. Fiederling, S. Kupfer, a) and S. Gräfeb)

Institut für Physikalische Chemie and Abbe Center of Photonics, Friedrich-Schiller-Universität Jena, Helmholtzweg 4, 07743 Jena, Germany

(Dated: June 23, 2021)

Experimental evidence suggests an extremely high, possibly even sub-molecular, spatial resolution of tipenhanced Raman spectroscopy (TERS). While the underlying mechanism is currently still under discussion, two main contributions are considered: The involved plasmonic particles are able to highly confine light to small spatial regions in the near-field, i.e. the electromagnetic effect, and the chemical effect due to altered molecular properties of the sample in close proximity to the plasmonic tip. Significant theoretical effort is put into the modelling of the electromagnetic contribution by various groups. In contrast, we previously introduced a computational protocol that allows for investigation of the local chemical effect – including nonresonant, resonant and charge transfer contributions – in a plasmonic hybrid system by mapping the sample molecule with a metallic tip model at the (time-dependent) density functional level of theory. In the present contribution, we evaluate the impact of static charges localized on the tip's frontmost atom, possibly induced by the tip geometry in the vicinity of the apex, on the TERS signal and the lateral resolution. To this aim, an immobilized molecule, i.e. tin(II) phthalocyanine (SnPc), is mapped by the plasmonic tip modeled by a single positively vs. negatively charged silver atom. The performed quantum chemical simulations reveal a pronounced enhancement of the Raman intensity under non-resonant and resonant conditions with respect to the uncharged reference system, while the contribution of charge transfer phenomena as well as of locally excited states of **SnPc** is highly dependent on the tip's charge.

I. INTRODUCTION

The ultimate goal of microscopy is to make the smallest things visible, and what could be smaller than the building blocks of matter: atoms and molecules. To achieve this goal, resolution in the Angstrom scale is necessary – but Abbe's diffraction limit is, for the visible spectrum of light, several orders of magnitude above this scale and therefore makes this seemingly impossible. However, some modern techniques are able to circumvent this limit through different means, like fluorescence-based stimulated emission depletion (STED), 1 photoactivated localization microscopy (PALM), 2 stochastic optical reconstruction microscopy (STORM), 3 and near-field methods like scanning near-field optical microscopy (SNOM), 4 and tip-enhanced Raman spectroscopy (TERS). 5–7

The mechanism behing TERS (and the closely related but not resolution-driven surface-enhanced Raman spectroscopy, SERS^{8–11}) is based on surface plasmons, leading to an increase in Raman signal by up to six orders of magnitude. ^{12,13} This is commonly attributed to two different effects: The electromagnetic effect ^{14–20} strongly increases the Raman signal of a sample close to the plasmonic particle by enhancing and confining the local electric field, especially in a so-called pico-cavity between the plasmonic tip and a metal substrate. ^{21–25} Furthermore, the field-induced dipole in the sample molecule is accompanied by a mirror dipole in the plasmonic particle, modifying and further enhancing the near-field. ^{26–28} On the other hand, the chemical effect ^{19,29–34} describes the

close-range interactions between the sample molecule and the plasmonic particle. Scanning the tip over the sample molecule leads to different site-specific tip-sample interaction and therefore can shift position and intensity of Raman bands, with extreme sensitivity to the local chemical environment. 20,35 The chemical effect is typically further divided into three parts: Ground-state contributions from non-resonant chemical interactions between tip and sample, resonant contributions due to excited states of the molecule with similar energy as the excitation radiation, and charge transfer phenomena between tip and sample. $^{19,31,36-39}$

Recent experiments under cryogenic and even ambient conditions hint at possible lateral resolutions of TERS of 1 nm or even below $^{40-47}$ and therefore providing up to (sub-)molecular resolution. At first this is surprising, considering that the employed plasmonic nanoparticles typically have a diameter of 20 to 40 nm. $^{48-51}$ Evidence suggests that small, atomic-sized features on the plasmonic particle are the source of this resolution 23,24,52,53 and deeper atomic layers in the particle play only a minor role. 35,54

several approaches to model There are example developed experiments, inthe for Jensen, $^{24,51,59-62}$ $Schatz, ^{55-58}$ groups of and Aizpurua. 11,22,40,52,53 The discrete model/quantum mechanical (DIM/QM) method^{27,28} by Jensen et al. provides a combination of timedependent density functional theory (TDDFT) for the sample molecule with atomistic electrodynamics simulation for the metallic particle. Aizpurua et al. and Sánchez-Portal et al. treat the plasmonic cavity on a full quantum electrodynamical level and thereby show that small, atomic-sized features on the nanoparticle

a) Electronic mail: stephan.kupfer@uni-jena.de

b) Electronic mail: s.graefe@uni-jena.de

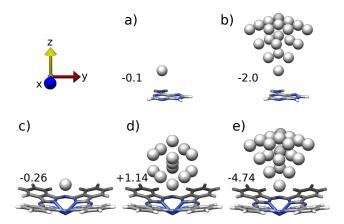


Figure 1. Mulliken charge of the apex tip atom for different tip models near adenine (a) single Ag atom, b) tetrahedral (Ag_{20}) cluster; from Ref. 35); or **SnPc**: c) single Ag atom, d) icosahedral (Ag_{13}) , e) tetrahedral (Ag_{20}) cluster.

can confine and enhance electromagnetic radiation into small enough volumes to provide sub-nanometer resolution. 52,53 Furthermore, by employing an effective Hamiltonian containing the highly confined electric field of a plasmonic particle, Luo et al. describe the tip-sample interaction quantum mechanically. $^{63-65}$

In another different approach, we introduced a computational protocol to describe highly location-specific tip-sample interactions entirely quantum chemically,³⁵ in essence covering the ground state contribution to the chemical effect. This model was expanded later on to also include excited-state and charge transfer phenomena by including the Raman response to light in resonance with molecular excited states.⁶⁶ To achieve this, the immobilized sample molecule is three-dimensionally mapped by placing a model of the plasmonic particle on different positions relative to the molecule. By constraining the tip model to a small cluster or even a single atom, this allows us to describe the whole hybrid system at a fairly high density functional theory (DFT) level and gives insight into the changes to molecular properties occuring by moving the tip in every possible spatial direction. Minute movements of the tip can result in large changes of spectral position and, especially, intensity of Raman bands, explaining the sub-molecular resolution. Excitation at resonant wavelengths on the other hand, provides a means to enhance the intensity of certain vibrational modes by several orders of magnitude, depending on the respective excited states in resonance.

In the current contribution, we elaborate on the influence of the charge of the frontmost (silver) tip atom on the ground and excited state properties of such plasmonic hybrid systems, and finally its impact on the local Raman response and the lateral resolution. This study is motivated by the observed variation of Raman signals and intensity maps of adenine mapped either by a single silver atom or a small tetrahedral cluster comprised of 20 silver atoms, see Fig. 1a) and b).³⁵ An analysis of

both neutral hybrid systems suggests that the polarizability is highly dependent on the charge of the Ag atom chemically interacting with the sample. Previous simulations show merely a small negative charge of -0.1efor the single-atom tip model. However, the silver cluster model features also a total charge of -0.1e in the hybrid system; its four vertices feature considerable negative partial charges, in particular – with -2.0e – the vertex chemically interacting with the sample. In addition, preliminary DFT results on various clusters models, i.e. an icosahedron (Ag_{13}) vs. a tetrahedron (Ag_{20}) shown in Fig. 1d) and e), suggest that positive as well as negative charges of the frontmost tip atom are present depending on the tip geometry – possibly influencing the chemical interaction and, thus, the TERS signal. Thus, the shape of the metallic nanoparticle might yield a specific chemical interaction in plasmon-enhanced spectroscopy. However, the interest in charged tips is not necessarily limited to theoretical investigations addressing structurally induced charge localization effects of the Raman signal, but charged tips may be introduced purposely in the experimental setup by applying an external electric potential. This way, the molecule's Raman signal can be obtained in the cavity of the tip and the immobilizing surface as a function of the applied voltage – resulting in (partially) charged tip atoms. ^{67,68} The chosen model system is similar to our previously studied one, consisting of an immobilized tin(II) phthalocyanine (SnPc) molecule that is mapped by a single, positively or negatively charged silver atom on the DFT and TDDFT level. In particular, we investigate singly positively vs. singly negatively charged silver tips in comparison to the uncharged reference. Planar molecules, such as (metallo-)porphyrins^{40,46,61,69,70} and phthalocyanines^{71–75} have been the subject of several studies in the context of plasmon-enhanced spectroscopy like SERS and TERS. SnPc in particular features bright excited states that can respond to light at different wavelengths and allows for possible charge transfer to or from the tip, both in the visible spectrum.

II. COMPUTATIONAL DETAILS

To simulate the tip-enhanced Raman spectroscopy (TERS) experiment, the same protocol as previously published by our group 35,66 was employed. In that, an immobilized molecule, i.e tin(II) phthalocyanine (\mathbf{SnPc}), is mapped by a silver tip, in this case modelled by a single silver atom, along a three-dimensional grid.

The geometry of the sample molecule, SnPc , was optimized and a vibrational analysis ensured that a minimum on the 3N-6 dimensional potential energy hypersurface has been obtained. The molecule was then oriented parallel to the x,y-plane, with the Sn atom localized in the origin of coordinates, and a single silver atom was placed on different 3D-positions above the sample, see Fig. 2. The z-coordinate (height) of the silver atom was chosen

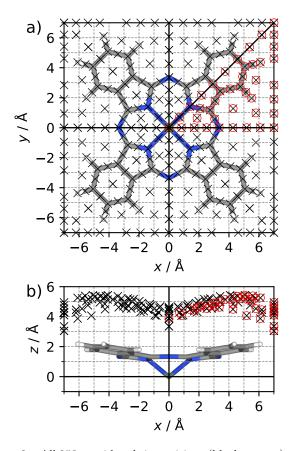


Figure 2. All 253 considered tip positions (black crosses) over the \mathbf{SnPc} molecule and the 41 explicitly calculated points (in red circles), as introduced previously. ⁶⁶ a) View along z-axis b) View along y-axis.

for each tip-position based on the van-der-Waals radii of SnPc and the silver atom; identical grids were applied for the charged hybrid systems. As shown previously by our group, 66 such van-der-Waals mapping allows to assess the local bonding region between the silver tip and the sample in reasonable agreement with computationally more demanding partial relaxations (x, y) coordinates frozen) within each position using density functional theory (DFT) calculations. Using the C_{4v} symmetry of the SnPc molecule, only 41 unique positions had to be considered explicitly, while the whole molecular map was obtained upon applying symmetry considerations. Additionally, the influence of the "height" (z-coordinate) of the silver tip above the molecule was studied exemplarily for two grid positions (see Fig. 4 and Fig. S5) in the range of 2.5 to 20 Å for the uncharged as well as for the charged tip mimics.

As a result of the unpaired electron in the silver atom (ground state electron configuration: $5s^14d^{10}$), the uncharged system is of doublet multiplicity with the spin density mainly residing in the 5s orbital of the silver atom; this hybrid system is denoted $\mathbf{SnPc-Ag}$. For the charged hybrid systems, the multiplicity was restricted to a singlet which localises the charge mainly on the silver

atom. These systems, featuring a positively or negatively charged tip, are labeled **SnPc-Ag**⁺ and **SnPc-Ag**⁻, respectively.

To assess the possible charge-induced lateral resolution limit of TERS – based on the chemical interaction among **SnPc** and the (charged) tip – 3D-grid simulations were performed, as outlined before. Therefore, on each position, the vibrational modes q_l including their polarizability derivatives $\partial \alpha/\partial q_l$ were calculated, as well as vertical excitation energies E_e , excited-state gradients $\partial E_e/\partial q_l$ and transition dipole moments μ_e for all relevant excited states e.

Contributions of all excited states within the excitation energy window of $0 < E_e \le 3.2\,\mathrm{eV}$ – corresponding to an excitation in the visible region – and with an oscillator strength of $f \ge 0.001$ were considered. Normal modes with a wavenumber of $\tilde{\nu}_l < 100\,\mathrm{cm}^{-1}$ were not taken into account.

Based on these properties, the independent-mode displaced harmonic oscillator model (IMDHOM) was employed. Here, it is assumed that the electronic ground-and excite- state potentials are harmonic and merely displaced in the equilibrium position and, hence, share the same set of vibrational modes. This allows calculating the zz-component of the transition polarizabilities as: 76

$$(\alpha_{zz})_{g0_l \to g1_l} = \sum_{e} (\mu_z)_e^2 \frac{\Delta_{e,l}}{\sqrt{2}} (\Phi_e(E_L) - \Phi_e(E_L - E_l)) .$$
(1)

With the dimensionless displacement $\Delta_{e,l}$, defined as:

$$\Delta_{e,l} = -\frac{\hbar^2}{\sqrt{E_l^3}} \left(\frac{\partial E_e}{\partial q_l}\right)_0 , \qquad (2)$$

and the function Φ_e , neglecting Franck-Condon factors, given by:

$$\Phi_e(E_{\rm L}) = \frac{1}{E_{e,g} - E_{\rm L} - i\Gamma}$$
(3)

In the equations above, $E_{e,g}$ is the vertical excitation energy from the ground-state g to excited-state e and Γ a damping factor describing homogeneous broadening (chosen as $3000\,\mathrm{cm}^{-1} \, \widehat{=} \, 0.372\,\mathrm{eV}$). Detailed information with respect to the computational methods has been previously reported. ^{66,76,77}

Assuming the detection of the Raman signal occurs mostly in z-direction (the direction of the metal tip), the intensity I_l of each mode is determined by the zz-component of the respective derivative of the (transition) polarizability tensor

$$I_{l} = \left(E_{L} - E_{l}\right)^{4} \left| \frac{\partial \left(\alpha_{zz}\right)_{g0_{l} \to g1_{l}}}{\partial q_{l}} \right|^{2}.$$
 (4)

All calculations were performed on the DFT and TDDFT levels of theory using the Gaussian 16 program⁷⁸ with the range-separated CAM-B3LYP functional⁷⁹ and

the 6-311+G** triple- ζ basis set.^{80,81} The metal atoms (tin, silver) were described with the electronic core potentials MWB46 and MWB28 and their respective basis sets⁸², respectively. The D3 dispersion correction with Becke-Johnson dampening was employed for all calculations.⁸³

III. RESULTS

This section elaborates on the simulated TERS response of both charged hybrid systems (i.e. SnPc-Ag⁺ and SnPc-Ag⁻) at the above mentioned level of theory, in comparison to the uncharged hybrid system (SnPc-Ag). First, the non-resonant case is discussed, observed for incident radiation with energy far away from any electronic excitations of the system, by employing exemplarily a 1064 nm laser. In the following, two laser wavelengths in the visible spectrum (633 nm and 442 nm) are chosen to probe the excited-state landscape and investigate different resonant Raman conditions. For a more detailed discussion of the uncharged SnPc-Ag system obtained using a similar computational protocol, see Ref. 66.

In part, results are presented in the form of intensity maps, where either the (resonant) TERS intensity of a certain mode is shown for different tip positions above the sample molecule, or the sum over the intensities of all modes. While the former gives more detailed insight which parts of the molecule respond in a certain, very narrow wavenumber region, the latter provides an overview over the general ability of the system to provide strong TERS responses for the different tip positions.

A. Non-resonant

Starting with the uncharged hybrid system, SnPc-Ag, there are three areas of high intensity that roughly form three concentric rings over the sample, as shown in Fig. 3a): The structure in the center of the molecule stems mostly from two low-wavenumber modes involving stretching of the inner C-N bonds (mode 90) as well as an out-of-plane vibration involving the whole molecule (mode 54). At this tip position, both modes have roughly the same intensity with 2.4×10^{-8} and 2.1×10^{-8} arb.u. respectively, and combined, they contribute to about a quarter of the overall intensity $(1.6 \times 10^{-7} \text{ arb.u.})$. The other two ring-like structures are mainly attributed to C-H in-plane modes and stretching of the outer C-N bonds. The middle structure follows the inner C-N ring of the molecule and heavily features a C-N-stretching vibration (mode 140) that alone contributes about a sixth $(3.0 \times 10^{-7} \, \text{arb.u.})$ to the overall intensity to the map. Other notable vibrations in this region (in order of decreasing intensity) stem from modes 133, 115, 116, and 103 (all C-H in-plane) with 2.2×10^{-7} , 2.2×10^{-7} , 1.8×10^{-7} , and 1.8×10^{-7} arb.u. intensity, respectively,

that combine to nearly half of this structure's brightness. Around the C-H bonds at the molecule's terminal, the third bright spot again originates from mode 140, but this time with less intensity (1.8×10^{-7} arb.u.). Additionally, modes 149 and 96, representing a ring deformation and a C-H stretching vibration, have their intensity maxima in this region and add to this relatively large region of high intensity.

In contrast, upon introduction of a charge at the tip, i.e. in case of $SnPc-Ag^+$ and $SnPc-Ag^-$, the contribution of C-H vibrations to the overall Raman signal generally decreases in favor of modes involving C-N bonds.

For the positively charged tip (SnPc-Ag⁺), this means that slightly lower wavenumber vibrations, especially those involving whole pyrrole rings, dominate the intensity map. The bright central spot in Fig. 3d) is mainly due to mode 107 [Fig. 3e), together with mode 106, see below which alone contributes 5.3×10^{-6} arb.u.. around a third of the overall intensity on this grid point. Modes 136, see Fig. 3f), and 106 (shown together with mode 107, as they are very close in wavenumbers) as the two next brightest ones with intensities of 3.1×10^{-6} and 2.3×10^{-6} arb.u. respectively together make up the second third of summed up intensity. All three modes involve vibrations of C-N bonds: mode 107 mainly involves the nitrogen atoms coordinating the central Sn atom, mode 136 in contrast distorts the C-N bonds connecting the isoindole moieties, and mode 106 is a stretching vibration of the pyrrole rings.

While in case of a positively charged tip, SnPc-Ag⁺, slightly lower wavenumbers modes, i.e. between 1150 and 1180 cm^{−1}, contribute most significantly, higher wavenumber modes $(1550 \text{ to } 1660 \text{ cm}^{-1})$ are most prominent for **SnPc-Ag**⁻. The intensity map in Fig. 3b) shows a broader intensity distribution mainly over the isoindole mioeties and the bridging N atoms between them. Even though this broad distribution involves several tip positions, only very few closely clustered modes make up the majority of the overall intensity, and all of them feature vibrations of the bridging C-N bonds. Mode 140 is the most intense one with 2.2×10^{-6} arb.u., followed by mode 142 $(1.7 \times 10^{-6} \text{ arb.u.})$, mode 144 $(1.5 \times 10^{-6} \text{ arb.u.})$, and mode 143 (1.4×10^{-6} arb.u.); since their wavenumbers are very close, their summed intensity is shown in Fig. 3c).

As evident from the integrated intensity maps, illustrated in Fig. 3a) vs. b) and d), over all modes, the overall intensity of the system's non-resonant TERS response increases by roughly two orders of magnitude after the introduction of a charge on the tip atom. This change is not only due to an intensity change in the few modes presented above, but rather drastically changes the whole spectrum of the **SnPc-Ag** hybrid system.

In case of the uncharged system, $\mathbf{SnPc-Ag}$, the tip-sample distance – based on van-der-Waals radii – is close to the minimum in the potential energy curve for a given xy-position of the tip mimic, ⁶⁶ see Fig. 4a) and Fig. S5 exemplarily. Notably, the potential energy curve

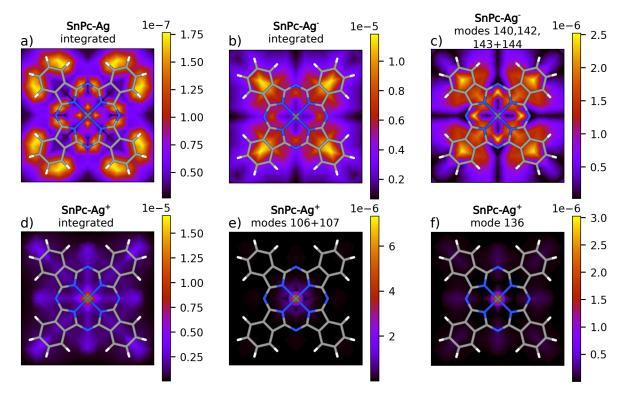


Figure 3. a) Integrated intensity map of the uncharged **SnPc-Ag** hybrid system b) integrated intensity map and c) map of modes 140, 142, 143, and 144 in the negatively charged hybrid system **SnPc-Ag** d) integrated intensity map, e) map of modes 106 and 107, and f) map of mode 136 in **SnPc-Ag**⁺.

of SnPc-Ag features two minima, the global minimum at roughly 3.9 Å results from the interacting of the silver atom with the central nitrogen atoms coordinating the tin, while the minimum at below 2 Å reveal the Ag-Sn interaction. However, with the introduced positive or negative charge, the bonding distance is altered for the respective hybrid systems. I.e., for both charged systems, the global minimum of the potential energy curve is shifted by roughly 1 Å to shorter distances, given by the Ag-Sn interaction, while in case of SnPc-Ag- the N-Ag minimum at 3.9 Å is still observed. For SnPc-Ag⁻, the binding energy between the molecule and the tip is comparable to the one of the uncharged system (0.37 and 0.47 eV, respectively) and the potential energy curve roughly follows the one from the uncharged system for greater tip-sample distances. However, the binding energy for the SnPc-Ag⁺ hybrid system is more than four times as large (2.00 eV) and therefore the curve is steeper, even for larger distances. For the TERS intensities shown in Fig. 4b), a roughly exponential increase was expected for smaller tip-sample separations. While for SnPc-Ag⁺ and SnPc-Ag, this behavior can be seen (except for very small distances), SnPc-Ag shows the opposite and decreases the intensity for small distances. A partial charge transfer in the ground state, as visible from the density differences of charged and uncharged systems in Fig. 4c), may explain the quenching of TERS intensity for small distances to a certain level.

B. Resonant

As previously shown for the uncharged hybrid system, $\pi\pi^*$ transitions of \mathbf{SnPc} are mainly x,y-polarized, i.e. in the molecular plane, and thus contribute only minor to the TERS signal observed in z-direction. Fig. 5 exemplarily shows for the lowest $\pi\pi^*$ state that these states are relatively insensitive to the position of the silver atom, both in terms of excitation energy (Fig. 5a)) and transition dipole moment (Fig. 5d)), recall Eq. 1. This also applies to $\mathbf{SnPc-Ag^+}$ (Fig. 5b) and e)) and $\mathbf{SnPc-Ag^-}$ (Fig. 5c) and f)), where these $\pi\pi^*$ states are barely affected neither by the positioning of the tip nor by its charge (see Fig. S1 and S2).

However, the charge transfer states – responsible for most of the Raman signal's contrast – respond strongly to the additional electron or hole on the silver atom. SnPc-Ag⁺ highly favors electron transfer from the molecule to the positively charged tip and thereby increases the number of low-lying ligand-to-metal charge transfer (LMCT) states with excitation energies below 3.5 eV from merely one in case of SnPc-Ag to about twelve (depending on the tip position) in SnPc-Ag⁺ (see Fig. S3 and S4). On the other hand, no metal-to-ligand charge transfer (MLCT) states could be identified in the same energy region.

The opposite is observed for **SnPc-Ag**⁻: No LMCT states below 3.5 eV are predicted by TDDFT, while the

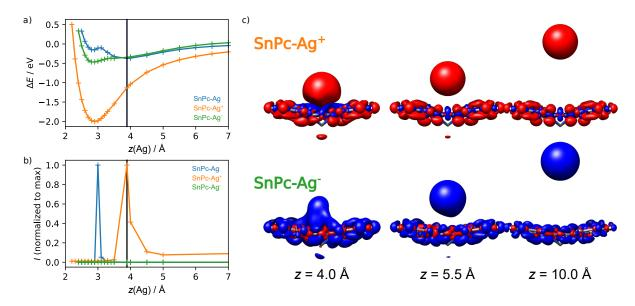


Figure 4. (a) Electric ground state potential energy curves ($\mathbf{SnPc-Ag}^+$ and $\mathbf{SnPc-Ag}^-$: singlet, $\mathbf{SnPc-Ag}$: doublet), (b) normalized TERS intensities and (c) density differences ($\rho_{\mathrm{charged}} - \rho_{\mathrm{neutral}}$) for selected z-positions, i.e. at z = 10, 5.5 and 4.0 Å, of the Ag tip mimic at the central position. The vertical black lines in (a) and (b) indicate the bonding region as approximated by the van-der-Waals radii.

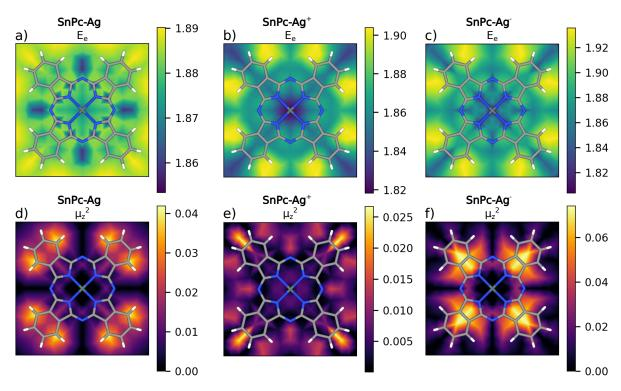


Figure 5. Excitation energies (a)-c); in eV) and squared transition dipole moments in z-direction μ_z^2 (d)-e); in a.u.) for the first $\pi\pi^*$ transition for different tip positions. a)+d) $\mathbf{SnPc-Ag}^+$ b)+e) $\mathbf{SnPc-Ag}^+$ c)+f) $\mathbf{SnPc-Ag}^-$.

number of MLCT states is increased from merely two (SnPc-Ag) to approximately 13 – depending on the tip's position. This behaviour was to be expected, as electron transfer to an already negatively charged atom is highly unfavourable due to Coulomb repulsion.

The lowest lying charge transfer states of SnPc-Ag⁺ and SnPc-Ag⁻ are (almost) degenerate with the electronic ground state. Thus, a charge transfer might even be possible within the electronic ground state, altering the character of the ground state upon chemical inter-

action of sample molecule and tip under (non-resonant) TERS conditions.

Furthermore, a couple of previously, i.e. SnPc-Ag, unencountered metal-centered (MC) transitions of the silver tip are predicted to contribute to the UV/vis spectra of the charged hybrid systems. For silver nanoparticles, such states are related to plasmonic states and contribute significantly to the TERS effect. However, excitation energies and transition dipole moments of such MC states are expected to be highly sensitive to the size as well as to the structure of the plasmonic nanoparticle. Thus, the contribution of silver MC states to the TERS effect are yet to be described correctly by our computational protocol. However, mapping sample molecules, e.g. SnPc, at the TDDFT level of theory with realistic metal clusters in a full quantum chemical fashion, which allows an unbiased describtion of the chemical effect, is currently computationally not feasable. Therefore, we omit a further discussion of these silver MC states in the present contribution.

In contrast to the non-resonant Raman effect, the wavelength of the incident light is crucial for resonance Raman since it determines which excited states contribute to the resonance enhancement. In this contribution, two irradiation wavelengths, namely 633 nm (1.96 eV) and 442 nm (2.81 eV), are studied exemplarily.

While in case of the uncharged **SnPc-Ag**, tip positions above the pyrrole C atoms stand out at 633 nm excitation (Fig. 6a)), for the **SnPc-Ag**⁺ hybrid system, the central point of the molecule stands out in intensity but this time about 4 orders of magnitude brighter than in the nonresonant TERS map (recall Fig. 3d)) with 0.35 arb.u., see Fig. 6f). This is due to an LMCT state representing an electron transfer from Ag to (mainly) Sn (see Fig. 7a) and c)) with a strong μ_z component and with an excitation energy of $\approx 1.5 \,\mathrm{eV}$ – in (partial) resonance with the exciting light source (see Fig. 6h)). The z-component of the transition dipole moment decreases at the neighboring grid points and vanishes quickly for positions away from the center. Most of the Raman intensity in the center originates from mode 128 (Fig. 6g)), a symmetric stretching of the central SnN₄-fragment, that alone contributes with an intensity of 0.33 arb.u. at this position.

In case of $\mathbf{SnPc-Ag^-}$, four wedge-like structures appear at the molecule's periphery (Fig. 6b)). The second $\pi\pi^*$ state, in resonance at 633 nm, distinctly features a high transition dipole moment in z-direction (Fig. 6e)) at those bright positions. This is attributed to the slightly upwards-facing benzene moieties that lead to the otherwise x,y polarized state to bleed into z-direction. Regarding the involved normal modes, the picture is more complex, as several modes contribute to the resonance Raman signal. The most intense modes are modes 143 (at 0.047 arb.u.) and 144 (0.026 arb.u., see their sum in Fig. 6c)), being stretching vibrations of the bridging C-N bonds, and mode 121 (Fig. 6d)) with 0.025 arb.u., a deformation of the pyrrole rings.

At 442 nm, the Raman intensity maximum for both the

 $\operatorname{SnPc-Ag}$ (Fig. 8a)) and the $\operatorname{SnPc-Ag^+}$ (Fig. 8d)) system is localised over the outer C_6 rings. For $\operatorname{SnPc-Ag^+}$ there is once more a LMCT transition with particularly high transition dipole moment in z-direction (Fig. 8f)) in resonance with the incident light at this position, and again, a single mode (mode 149 at 11.7 arb.u.) is responsible for most of the overall intensity of 14 arb.u. (Fig. 8e)). This mode represents a ring deformation of the C_6 ring(s), particularly the one directly below the tip.

As in all discussed scenarios, introducing a charge on the frontmost tip atom significantly alters and enhances the overall intensity of the system's resonance Raman response. However, in case of the negatively charged tip in SnPc-Ag⁻ and excitation at 442 nm, the signal enhancement is orders of magnitude higher, especially at the periphery of the molecule in the form of a bright band-like structure in Fig. 8b). Comparable to the system under 633 nm illumination, a $\pi\pi^*$ state (see Fig. 7b)) is in resonance and its typical polarization in the molecular plane is visible in z-direction due to a particlularly large μ_z (Fig. 8c)) at those positions because of the slight upwards tilt of the benzene rings. The $\pi\pi^*$ state features a distinctly high dimensionless displacement, $\Delta_{e,l}$ (recall Eq.1), as a result of its pronounced excited state gradient within the Franck-Condon point, along a small number of normal modes across the spectrum. All of these modes show similar intensity maps as the summed map in Fig. 8b).

IV. CONCLUSION

In this contribution, we extend our computational protocol that is able to simulate all three contributions non-resonant, resonant and charge transfer – of the chemical effect in a full quantum chemical approach to also include a static charge on the plasmonic tip. Thereby, the introduced positive or negative charge reflects the impact on the charge distribution, as predicted for various tip geometries, on the tip's frontmost atom chemically interacting with the sample. We investigated a sample molecule, tin(II) phthalocyanine (SnPc), by scanning it with a single, charged silver atom as a tip mimic and observed its TERS response under different, resonant and non-resonant, conditions to further investigate the source of the proposed sub-molecular resolution. The system was described by DFT and TDDFT and the Raman response was obtained in z-direction; however in principle, the approach can be generalized to other levels of theory and include other illumination-observation geometries.

Under non-resonant irradiation, the hybrid system already reacts strongly to the introduced charge as the overall signal intensity increases by two orders of magnitude. While for the previously studied, uncharged hybrid system either C-H bending or C-N stretching modes dominate the spectra for different tip positions, ⁶⁶ C-H modes lose importance for the charged systems. For a positive

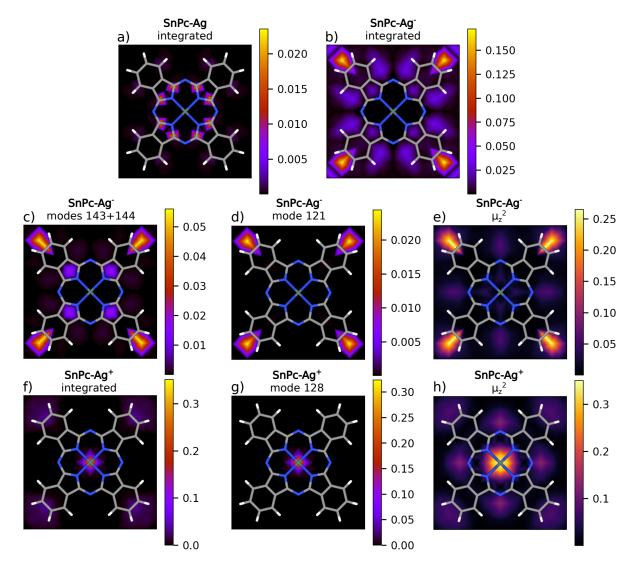


Figure 6. Maps for incident radiation at 633 nm. a) Integrated intensity map of $\mathbf{SnPc\text{-}Ag}$ b) integrated intensity map, c) map of modes 143 and 144, d) map of mode 121, and e) μ_z^2 of the second $\pi\pi^*$ state in $\mathbf{SnPc\text{-}Ag}$ (in a.u.) f) integrated intensity map, g) map of mode 128, and h) μ_z^2 of the second LMCT state in $\mathbf{SnPc\text{-}Ag}$ (in a.u.).

tip, this leads to a single vibration that dominates the intensity map and is able to accurately pinpoint tip positions over the center of the molecule. For a negatively charged tip, on the other hand, mostly positions over the extended π system of the isoindole moieties provide the highest intensities, this time for several modes involving mainly vibrations of the inner C-N ring.

The general increase in signal intensity after introduction of the charge is observed for resonant excitation as well. The excited state landscape is changed drastically, however, the molecule's $\pi\pi^*$ states mostly remain unaffected, as several new charge transfer states are introduced. A single molecule-to-tip charge transfer state dominates in the positively charged hybrid system for both studied wavelengths. For low-energy excitation either again positions over the molecule's center are highlighted (as the charge is transferred primarily from the

central Sn atom), or, in the high-energy regime, tip positions over the outwards-facing parts of the benzene rings.

The strongest resonant TERS response is achieved in case of a negative charge on the tip atom. Here, albeit charge transfer states appear as numerously as in the positive case with opposite directionality, $\pi\pi^*$ states are responsible for the tremendous increase in signal. While they only played minor roles in the uncharged and positive cases, their transition dipole moment gains a significant component in z-direction (μ_z) , especially over the slightly upwards tilted outer benzene rings.

Generally, it could be shown that the Raman response of a molecular-plasmonic hybrid system is highly dependent on the tip's position as well as on its charge. In addition, the introduction of both a negative or positive charge at the tip's apex alters the region of strongest chemical interactions among the tip mimic and

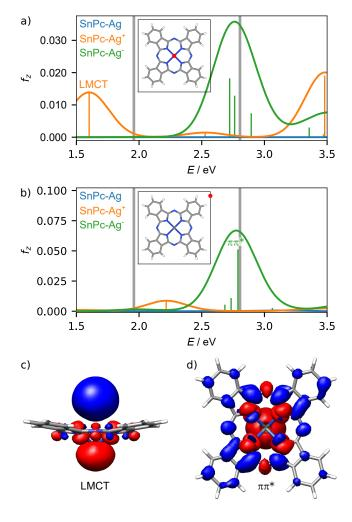


Figure 7. a) and b) z-polarized UV/vis spectra of $\mathbf{SnPc\text{-}Ag}$, $\mathbf{SnPc\text{-}Ag}^+$ and $\mathbf{SnPc\text{-}Ag}^-$ at selected tip positions, see insets. These positions, a) and b), feature the maximum TERS intensity of $\mathbf{SnPc\text{-}Ag}^+$ at 633 nm and $\mathbf{SnPc\text{-}Ag}^-$ at 442 nm excitation, respectively, see Fig. 6f) and Fig. 8b); excitation energies (1.96 and 2.81 eV, 633 and 442 nm) are indicated by grey vertical lines. Charge density differences for the labelled states: c) ligand-to-metal charge transfer (LMCT) with partial contribution of the Sn atom's 5s orbital (side view) and d) $\pi\pi^*$ (top view).

the molecule. In case of the present hybrid systems, this was observed particularly for $\mathbf{SnPc\text{-}Ag^+}$ – favoring much shorter bonding distances and considerably higher binding energies in comparison to $\mathbf{SnPc\text{-}Ag}$.

The incorporation of the electromagnetic effect in the form of more complex fields is the point of interest of ongoing studies, under non-resonant and resonant conditions, as is the addition of the immobilizing surface.

SUPPLEMENTARY MATERIAL

See supplementary material for excitation energy and transition dipole moment maps of selected $\pi\pi^*$, ligand-to-metal charge transfer and metal-to-ligand charge transfer states as well as potential energies curves and normalized Raman intensities along the z-coordinate for the charged and uncharged hybrid systems

ACKNOWLEDGEMENTS

The authors gratefully acknowledge funding from the European Research Council (ERC) under the European's Horizon 2020 research and innovation programme – QUEM-CHEM (grant number 772676), "Time- and space-resolved ultrafast dynamics in molecular plasmonic hybrid systems". This work was further funded by the Deutsche Forschungsgemeinschaft (DFG, German Research Foundation) – project number A4 – SFB 1375. All calculations were performed at the Universitätsrechenzentrum of the Friedrich Schiller University Jena.

AIP PUBLISHING DATA SHARING POLICY

The data that support the findings of this study are available from the corresponding author upon reasonable request.

REFERENCES

¹S. W. Hell and J. Wichmann, "Breaking the diffraction resolution limit by stimulated emission: Stimulated-emission-depletion fluorescence microscopy," Optics Letters **19**, 780–782 (1994).

²E. Betzig, G. H. Patterson, R. Sougrat, O. W. Lindwasser, S. Olenych, J. S. Bonifacino, M. W. Davidson, J. Lippincott-Schwartz, and H. F. Hess, "Imaging Intracellular Fluorescent Proteins at Nanometer Resolution," Science 313, 1642–1645 (2006).

³M. J. Rust, M. Bates, and X. Zhuang, "Sub-diffraction-limit imaging by stochastic optical reconstruction microscopy (STORM)," Nature Methods **3**, 793–796 (2006).

⁴E. A. Ash and G. Nicholls, "Super-resolution Aperture Scanning Microscope," Nature **237**, 510–512 (1972).

⁵M. S. Anderson, "Locally enhanced Raman spectroscopy with an atomic force microscope," Applied Physics Letters **76**, 3130–3132 (2000).

⁶N. Hayazawa, Y. Inouye, Z. Sekkat, and S. Kawata, "Metallized tip amplification of near-field Raman scattering," Optics Communications 183, 333–336 (2000).

⁷R. M. Stöckle, Y. D. Suh, V. Deckert, and R. Zenobi, "Nanoscale chemical analysis by tip-enhanced Raman spectroscopy," Chemical Physics Letters 318, 131–136 (2000).

⁸M. Fleischmann, P. J. Hendra, and A. J. McQuillan, "Raman spectra of pyridine adsorbed at a silver electrode," Chemical Physics Letters 26, 163–166 (1974).

⁹M. G. Albrecht and J. A. Creighton, "Anomalously intense Raman spectra of pyridine at a silver electrode," Journal of the American Chemical Society 99, 5215–5217 (1977).

¹⁰D. L. Jeanmaire and R. P. Van Duyne, "Surface raman spectroelectrochemistry: Part I. Heterocyclic, aromatic, and aliphatic

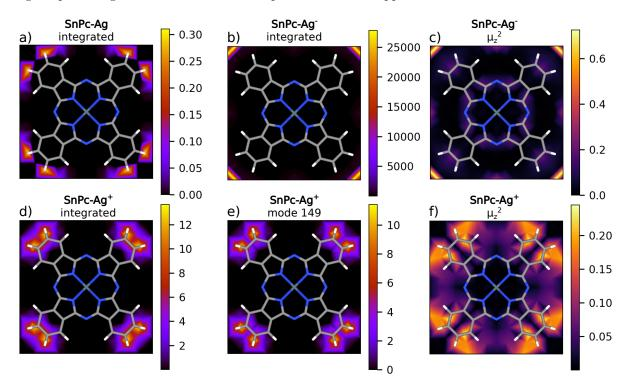


Figure 8. Maps for incident radiation at 442 nm. a) Integrated intensity map of **SnPc-Ag** b) integrated intensity map and c) μ_z^2 of the fourth $\pi\pi^*$ state in **SnPc-Ag** (in a.u.) d) integrated intensity map, e) map of mode 149, and f) μ_z^2 of the fifth LMCT state in **SnPc-Ag**⁺ (in a.u.).

amines adsorbed on the anodized silver electrode," Journal of Electroanalytical Chemistry and Interfacial Electrochemistry $\bf 84$, 1-20 (1977).

¹¹ J. Langer, D. Jimenez de Aberasturi, J. Aizpurua, R. A. Alvarez-Puebla, B. Auguié, J. J. Baumberg, G. C. Bazan, S. E. J. Bell, A. Boisen, A. G. Brolo, J. Choo, D. Cialla-May, V. Deckert, L. Fabris, K. Faulds, F. J. García de Abajo, R. Goodacre, D. Graham, A. J. Haes, C. L. Haynes, C. Huck, T. Itoh, M. Käll, J. Kneipp, N. A. Kotov, H. Kuang, E. C. Le Ru, H. K. Lee, J.-F. Li, X. Y. Ling, S. A. Maier, T. Mayerhöfer, M. Moskovits, K. Murakoshi, J.-M. Nam, S. Nie, Y. Ozaki, I. Pastoriza-Santos, J. Perez-Juste, J. Popp, A. Pucci, S. Reich, B. Ren, G. C. Schatz, T. Shegai, S. Schlücker, L.-L. Tay, K. G. Thomas, Z.-Q. Tian, R. P. Van Duyne, T. Vo-Dinh, Y. Wang, K. A. Willets, C. Xu, H. Xu, Y. Xu, Y. S. Yamamoto, B. Zhao, and L. M. Liz-Marzán, "Present and Future of Surface-Enhanced Raman Scattering," ACS Nano 14, 28–117 (2020).

¹²N. Jiang, E. T. Foley, J. M. Klingsporn, M. D. Sonntag, N. A. Valley, J. A. Dieringer, T. Seideman, G. C. Schatz, M. C. Hersam, and R. P. Van Duyne, "Observation of Multiple Vibrational Modes in Ultrahigh Vacuum Tip-Enhanced Raman Spectroscopy Combined with Molecular-Resolution Scanning Tunneling Microscopy," Nano Letters 12, 5061–5067 (2012).

¹³B. Pettinger, B. Ren, G. Picardi, R. Schuster, and G. Ertl, "Nanoscale Probing of Adsorbed Species by Tip-Enhanced Raman Spectroscopy," Physical Review Letters 92, 096101 (2004).

¹⁴S. Corni and J. Tomasi, "Theoretical evaluation of Raman spectra and enhancement factors for a molecule adsorbed on a complex-shaped metal particle," Chemical Physics Letters 342, 135–140 (2001).

¹⁵S. Corni and J. Tomasi, "Surface enhanced Raman scattering from a single molecule adsorbed on a metal particle aggregate: A theoretical study," The Journal of Chemical Physics 116, 1156– 1164 (2001). ¹⁶D. V. Chulhai and L. Jensen, "Determining Molecular Orientation With Surface-Enhanced Raman Scattering Using Inhomogenous Electric Fields," The Journal of Physical Chemistry C 117, 19622–19631 (2013).

¹⁷N. Chiang, N. Jiang, D. V. Chulhai, E. A. Pozzi, M. C. Hersam, L. Jensen, T. Seideman, and R. P. Van Duyne, "Molecular-Resolution Interrogation of a Porphyrin Monolayer by Ultrahigh Vacuum Tip-Enhanced Raman and Fluorescence Spectroscopy," Nano Letters 15, 4114–4120 (2015).

¹⁸C. Zhang, B.-Q. Chen, and Z.-Y. Li, "Optical Origin of Subnanometer Resolution in Tip-Enhanced Raman Mapping," The Journal of Physical Chemistry C 119, 11858–11871 (2015).

¹⁹S. M. Morton, D. W. Silverstein, and L. Jensen, "Theoretical Studies of Plasmonics using Electronic Structure Methods," Chemical Reviews 111, 3962–3994 (2011).

²⁰M. Thomas, S. Mühlig, T. Deckert-Gaudig, C. Rockstuhl, V. Deckert, and P. Marquetand, "Distinguishing chemical and electromagnetic enhancement in surface-enhanced Raman spectra: The case of para-nitrothiophenol," Journal of Raman Spectroscopy 44, 1497–1505 (2013).

²¹P. Zhang, J. Feist, A. Rubio, P. García-González, and F. J. García-Vidal, "Ab initio nanoplasmonics: The impact of atomic structure," Physical Review B 90, 161407 (2014).

²²F. Benz, M. K. Schmidt, A. Dreismann, R. Chikkaraddy, Y. Zhang, A. Demetriadou, C. Carnegie, H. Ohadi, B. de Nijs, R. Esteban, J. Aizpurua, and J. J. Baumberg, "Single-molecule optomechanics in "picocavities"," Science 354, 726–729 (2016).

²³S. Trautmann, J. Aizpurua, I. Götz, A. Undisz, J. Dellith, H. Schneidewind, M. Rettenmayr, and V. Deckert, "A classical description of subnanometer resolution by atomic features in metallic structures," Nanoscale 9, 391–401 (2016).

²⁴X. Chen and L. Jensen, "Morphology dependent near-field response in atomistic plasmonic nanocavities," Nanoscale 10, 11410–11417 (2018).

- ²⁵M. Urbieta, M. Barbry, Y. Zhang, P. Koval, D. Sánchez-Portal, N. Zabala, and J. Aizpurua, "Atomic-Scale Lightning Rod Effect in Plasmonic Picocavities: A Classical View to a Quantum Effect," ACS Nano 12, 585–595 (2018).
- ²⁶T. Atay, J.-H. Song, and A. V. Nurmikko, "Strongly Interacting Plasmon Nanoparticle Pairs: From Dipole-Dipole Interaction to Conductively Coupled Regime," Nano Letters 4, 1627–1631 (2004).
- ²⁷S. M. Morton and L. Jensen, "A discrete interaction model/quantum mechanical method for describing response properties of molecules adsorbed on metal nanoparticles," The Journal of Chemical Physics 133, 074103 (2010).
- ²⁸S. M. Morton and L. Jensen, "A discrete interaction model/quantum mechanical method to describe the interaction of metal nanoparticles and molecular absorption," The Journal of Chemical Physics 135, 134103 (2011).
- ²⁹Zhao, L. Jensen, and G. C. Schatz, "Pyridine-Ag20 Cluster: A Model System for Studying Surface-Enhanced Raman Scattering," Journal of the American Chemical Society 128, 2911–2919 (2006).
- ³⁰L. Jensen, L. L. Zhao, and G. C. Schatz, "Size-Dependence of the Enhanced Raman Scattering of Pyridine Adsorbed on Agn (n = 2-8, 20) Clusters," The Journal of Physical Chemistry C 111, 4756–4764 (2007).
- ³¹L. Jensen, C. M. Aikens, and G. C. Schatz, "Electronic structure methods for studying surface-enhanced Raman scattering," Chemical Society Reviews 37, 1061–1073 (2008).
- ³²S. Liu, X. Zhao, Y. Li, M. Chen, and M. Sun, "DFT study of adsorption site effect on surface-enhanced Raman scattering of neutral and charged pyridine—Ag4 complexes," Spectrochimica Acta Part A: Molecular and Biomolecular Spectroscopy 73, 382— 387 (2009).
- ³³N. Valley, N. Greeneltch, R. P. Van Duyne, and G. C. Schatz, "A Look at the Origin and Magnitude of the Chemical Contribution to the Enhancement Mechanism of Surface-Enhanced Raman Spectroscopy (SERS): Theory and Experiment," The Journal of Physical Chemistry Letters 4, 2599–2604 (2013).
- ³⁴F. Latorre, J. Guthmuller, and P. Marquetand, "A spectroscopic study of the cis/trans-isomers of penta-2,4-dienoic acid attached to gold nanoclusters," Physical Chemistry Chemical Physics 17, 7648–7658 (2015).
- ³⁵F. Latorre, S. Kupfer, T. Bocklitz, D. Kinzel, S. Trautmann, S. Gräfe, and V. Deckert, "Spatial resolution of tip-enhanced Raman spectroscopy – DFT assessment of the chemical effect," Nanoscale 8, 10229–10239 (2016).
- ³⁶M. Sun, Y. Fang, Z. Yang, and H. Xu, "Chemical and electromagnetic mechanisms of tip-enhanced Raman scattering," Physical Chemistry Chemical Physics 11, 9412–9419 (2009).
- ³⁷F. Avila, D. J. Fernandez, J. F. Arenas, J. C. Otero, and J. Soto, "Modelling the effect of the electrode potential on the metal-adsorbate surface states: Relevant states in the charge transfer mechanism of SERS," Chemical Communications 47, 4210–4212 (2011).
- ³⁸F. Avila, C. Ruano, I. Lopez-Tocon, J. F. Arenas, J. Soto, and J. C. Otero, "How the electrode potential controls the selection rules of the charge transfer mechanism of SERS," Chemical Communications 47, 4213–4215 (2011).
- ³⁹L. Xia, M. Chen, X. Zhao, Z. Zhang, J. Xia, H. Xu, and M. Sun, "Visualized method of chemical enhancement mechanism on SERS and TERS," Journal of Raman Spectroscopy 45, 533–540 (2014).
- ⁴⁰R. Zhang, Y. Zhang, Z. C. Dong, S. Jiang, C. Zhang, L. G. Chen, L. Zhang, Y. Liao, J. Aizpurua, Y. Luo, J. L. Yang, and J. G. Hou, "Chemical mapping of a single molecule by plasmon-enhanced Raman scattering," Nature 498, 82–86 (2013).
- ⁴¹Y. Fang, Z. Zhang, L. Chen, and M. Sun, "Near field plasmonic gradient effects on high vacuum tip-enhanced Raman spectroscopy," Physical Chemistry Chemical Physics 17, 783–794 (2014).

- ⁴²J. M. Klingsporn, N. Jiang, E. A. Pozzi, M. D. Sonntag, D. Chulhai, T. Seideman, L. Jensen, M. C. Hersam, and R. P. V. Duyne, "Intramolecular Insight into Adsorbate—Substrate Interactions via Low-Temperature, Ultrahigh-Vacuum Tip-Enhanced Raman Spectroscopy," Journal of the American Chemical Society 136, 3881–3887 (2014).
- ⁴³M. Sun, Z. Zhang, L. Chen, S. Sheng, and H. Xu, "Plasmonic Gradient Effects on High Vacuum Tip-Enhanced Raman Spectroscopy," Advanced Optical Materials 2, 74–80 (2014).
- ⁴⁴Z. He, Z. Han, M. Kizer, R. J. Linhardt, X. Wang, A. M. Sinyukov, J. Wang, V. Deckert, A. V. Sokolov, J. Hu, and M. O. Scully, "Tip-Enhanced Raman Imaging of Single-Stranded DNA with Single Base Resolution," Journal of the American Chemical Society 141, 753–757 (2019).
- ⁴⁵S. Jiang, Y. Zhang, R. Zhang, C. Hu, M. Liao, Y. Luo, J. Yang, Z. Dong, and J. G. Hou, "Distinguishing adjacent molecules on a surface using plasmon-enhanced Raman scattering," Nature Nanotechnology 10, 865–869 (2015).
- ⁴⁶ J. Lee, K. T. Crampton, N. Tallarida, and V. A. Apkarian, "Visualizing vibrational normal modes of a single molecule with atomically confined light," Nature 568, 78–82 (2019).
- ⁴⁷M. Richard-Lacroix, Y. Zhang, Z. Dong, and V. Deckert, "Mastering high resolution tip-enhanced Raman spectroscopy: Towards a shift of perception," Chemical Society Reviews 46, 3922–3944 (2017).
- ⁴⁸Y. C. Martin, H. F. Hamann, and H. K. Wickramasinghe, "Strength of the electric field in apertureless near-field optical microscopy," Journal of Applied Physics 89, 5774–5778 (2001).
- ⁴⁹P. I. Geshev, S. Klein, T. Witting, K. Dickmann, and M. Hietschold, "Calculation of the electric-field enhancement at nanoparticles of arbitrary shape in close proximity to a metallic surface," Physical Review B 70, 075402 (2004).
- ⁵⁰I. Notingher and A. Elfick, "Effect of Sample and Substrate Electric Properties on the Electric Field Enhancement at the Apex of SPM Nanotips," The Journal of Physical Chemistry B 109, 15699–15706 (2005).
- ⁵¹J. L. Payton, S. M. Morton, J. E. Moore, and L. Jensen, "A Hybrid Atomistic Electrodynamics—Quantum Mechanical Approach for Simulating Surface-Enhanced Raman Scattering," Accounts of Chemical Research 47, 88–99 (2014).
- ⁵²M. Barbry, P. Koval, F. Marchesin, R. Esteban, A. G. Borisov, J. Aizpurua, and D. Sánchez-Portal, "Atomistic Near-Field Nanoplasmonics: Reaching Atomic-Scale Resolution in Nanooptics," Nano Letters 15, 3410–3419 (2015).
- ⁵³M. K. Schmidt, R. Esteban, A. González-Tudela, G. Giedke, and J. Aizpurua, "Quantum Mechanical Description of Raman Scattering from Molecules in Plasmonic Cavities," ACS Nano 10, 6291–6298 (2016).
- ⁵⁴S. Trautmann, M. Richard-Lacroix, A. Dathe, H. Schneidewind, J. Dellith, W. Fritzsche, and V. Deckert, "Plasmon response evaluation based on image-derived arbitrary nanostructures," Nanoscale 10, 9830–9839 (2018).
- ⁵⁵E. Hao and G. C. Schatz, "Electromagnetic fields around silver nanoparticles and dimers," The Journal of Chemical Physics 120, 357–366 (2003).
- ⁵⁶S. Zou, N. Janel, and G. C. Schatz, "Silver nanoparticle array structures that produce remarkably narrow plasmon lineshapes," The Journal of Chemical Physics 120, 10871–10875 (2004).
- ⁵⁷R. L. Gieseking, M. A. Ratner, and G. C. Schatz, "Semiempirical Modeling of Ag Nanoclusters: New Parameters for Optical Property Studies Enable Determination of Double Excitation Contributions to Plasmonic Excitation," The Journal of Physical Chemistry A 120, 4542–4549 (2016).
- ⁵⁸W. Ding, L.-Y. Hsu, C. W. Heaps, and G. C. Schatz, "Plasmon-Coupled Resonance Energy Transfer II: Exploring the Peaks and Dips in the Electromagnetic Coupling Factor," The Journal of Physical Chemistry C 122, 22650–22659 (2018).
- ⁵⁹ J. L. Payton, S. M. Morton, J. E. Moore, and L. Jensen, "A discrete interaction model/quantum mechanical method for simulating surface-enhanced Raman spectroscopy," The Journal of

- Chemical Physics 136, 214103 (2012).
- ⁶⁰Z. Hu, D. V. Chulhai, and L. Jensen, "Simulating Surface-Enhanced Hyper-Raman Scattering Using Atomistic Electrodynamics-Quantum Mechanical Models," Journal of Chemical Theory and Computation 12, 5968–5978 (2016).
- ⁶¹P. Liu, D. V. Chulhai, and L. Jensen, "Single-Molecule Imaging Using Atomistic Near-Field Tip-Enhanced Raman Spectroscopy," ACS Nano 11, 5094–5102 (2017).
- ⁶²X. Chen, P. Liu, Z. Hu, and L. Jensen, "High-resolution tip-enhanced Raman scattering probes sub-molecular density changes," Nature Communications 10, 2567 (2019).
- ⁶³S. Duan, G. Tian, Y. Ji, J. Shao, Z. Dong, and Y. Luo, "Theoretical Modeling of Plasmon-Enhanced Raman Images of a Single Molecule with Subnanometer Resolution," Journal of the American Chemical Society 137, 9515–9518 (2015).
- ⁶⁴S. Duan, G. Tian, and Y. Luo, "Visualization of Vibrational Modes in Real Space by Tip-Enhanced Non-Resonant Raman Spectroscopy," Angewandte Chemie International Edition 55, 1041–1045 (2016).
- ⁶⁵Z. Xie, S. Duan, G. Tian, C.-K. Wang, and Y. Luo, "Theoretical modeling of tip-enhanced resonance Raman images of switchable azobenzene molecules on Au(111)," Nanoscale 10, 11850–11860 (2018).
- ⁶⁶K. Fiederling, M. Abasifard, M. Richter, V. Deckert, S. Gräfe, and S. Kupfer, "The chemical effect goes resonant a full quantum mechanical approach on TERS," Nanoscale 12, 6346–6359 (2020).
- ⁶⁷J. Lee, N. Tallarida, X. Chen, L. Jensen, and V. A. Apkarian, "Microscopy with a single-molecule scanning electrometer," Science Advances 4, eaat5472 (2018).
- ⁶⁸D. Peller, C. Roelcke, L. Z. Kastner, T. Buchner, A. Neef, J. Hayes, F. Bonafé, D. Sidler, M. Ruggenthaler, A. Rubio, R. Huber, and J. Repp, "Quantitative sampling of atomic-scale electromagnetic waveforms," Nature Photonics, 1–5 (2020).
- ⁶⁹L. Meng, Z. Yang, J. Chen, and M. Sun, "Effect of Electric Field Gradient on Sub-nanometer Spatial Resolution of Tip-enhanced Raman Spectroscopy," Scientific Reports 5, 9240 (2015).
- ⁷⁰N. Chiang, X. Chen, G. Goubert, D. V. Chulhai, X. Chen, E. A. Pozzi, N. Jiang, M. C. Hersam, T. Seideman, L. Jensen, and R. P. Van Duyne, "Conformational Contrast of Surface-Mediated Molecular Switches Yields Ångstrom-Scale Spatial Resolution in Ultrahigh Vacuum Tip-Enhanced Raman Spectroscopy," Nano Letters 16, 7774–7778 (2016).
- ⁷¹C. Stadler, S. Hansen, I. Kröger, C. Kumpf, and E. Umbach, "Tuning intermolecular interaction in long-range-ordered submonolayer organic films," Nature Physics 5, 153–158 (2009).
- ⁷²I. Kröger, B. Stadtmüller, C. Stadler, J. Ziroff, M. Kochler, A. Stahl, F. Pollinger, T.-L. Lee, J. Zegenhagen, F. Reinert, and C. Kumpf, "Submonolayer growth of copper-phthalocyanine on Ag(111)," New Journal of Physics 12, 083038 (2010).
- ⁷³B. Birmingham, Z. Liege, N. Larson, W. Lu, K. T. Park, H. W. H. Lee, D. V. Voronine, M. O. Scully, and Z. Zhang, "Probing Interaction between Individual Submonolayer Nanoislands and Bulk MoS2 Using Ambient TERS," The Journal of Physical Chemistry

- C **122**, 2753–2760 (2018).
- ⁷⁴R. B. Jaculbia, H. Imada, K. Miwa, T. Iwasa, M. Takenaka, B. Yang, E. Kazuma, N. Hayazawa, T. Taketsugu, and Y. Kim, "Single-molecule resonance Raman effect in a plasmonic nanocavity," Nature Nanotechnology 15, 105–110 (2020).
- ⁷⁵R. Jaculbia, N. Hayazawa, H. Imada, and Y. Kim, "Controlling the Resonance Raman Effect in Tip-Enhanced Raman Spectroscopy Using a Thin Insulating Film," Applied Spectroscopy **74**, 1391–1397 (2020).
- ⁷⁶J. Guthmuller, "Comparison of simplified sum-over-state expressions to calculate resonance Raman intensities including Franck-Condon and Herzberg-Teller effects," The Journal of Chemical Physics **144**, 064106 (2016).
- ⁷⁷M. Wächtler, J. Guthmuller, L. González, and B. Dietzek, "Analysis and characterization of coordination compounds by resonance Raman spectroscopy," Coordination Chemistry Reviews 19th International Symposium on the Photophysics and Photochemistry of Coordination Compounds, 256, 1479–1508 (2012).
- ⁷⁸M. J. Frisch, G. W. Trucks, H. B. Schlegel, G. E. Scuseria, M. A. Robb, J. R. Cheeseman, G. Scalmani, V. Barone, G. A. Petersson, H. Nakatsuji, X. Li, M. Caricato, A. V. Marenich, J. Bloino, B. G. Janesko, R. Gomperts, B. Mennucci, H. P. Hratchian, J. V. Ortiz, A. F. Izmaylov, J. L. Sonnenberg, D. Williams-Young, F. Ding, F. Lipparini, F. Egidi, J. Goings, B. Peng, A. Petrone, T. Henderson, D. Ranasinghe, V. G. Zakrzewski, J. Gao, N. Rega, G. Zheng, W. Liang, M. Hada, M. Ehara, K. Toyota, R. Fukuda, J. Hasegawa, M. Ishida, T. Nakajima, Y. Honda, O. Kitao, H. Nakai, T. Vreven, K. Throssell, J. A. Montgomery, Jr., J. E. Peralta, F. Ogliaro, M. J. Bearpark, J. J. Heyd, E. N. Brothers, K. N. Kudin, V. N. Staroverov, T. A. Keith, R. Kobayashi, J. Normand, K. Raghavachari, A. P. Rendell, J. C. Burant, S. S. Iyengar, J. Tomasi, M. Cossi, J. M. Millam, M. Klene, C. Adamo, R. Cammi, J. W. Ochterski, R. L. Martin, K. Morokuma, O. Farkas, J. B. Foresman, and D. J. Fox, "Gaussian 16 Revision B.01," (2016).
- ⁷⁹T. Yanai, D. P. Tew, and N. C. Handy, "A new hybrid exchange-correlation functional using the Coulomb-attenuating method (CAM-B3LYP)," Chemical Physics Letters 393, 51–57 (2004).
- ⁸⁰R. Krishnan, J. S. Binkley, R. Seeger, and J. A. Pople, "Self-consistent molecular orbital methods. XX. A basis set for correlated wave functions," The Journal of Chemical Physics 72, 650–654 (1980).
- ⁸¹T. Clark, J. Chandrasekhar, G. W. Spitznagel, and P. V. R. Schleyer, "Efficient diffuse function-augmented basis sets for anion calculations. III. The 3-21+G basis set for first-row elements, Li-F," Journal of Computational Chemistry 4, 294–301 (1983).
- ⁸²D. Andrae, U. Häußermann, M. Dolg, H. Stoll, and H. Preuß, "Energy-adjusted ab initio pseudopotentials for the second and third row transition elements," Theoretica chimica acta 77, 123– 141 (1990).
- ⁸³S. Grimme, S. Ehrlich, and L. Goerigk, "Effect of the damping function in dispersion corrected density functional theory," Journal of Computational Chemistry 32, 1456–1465 (2011).